PHYSICAL REVIEW B **113**, 014304 (2026)

Editors' Suggestion

Ultrafast modification of coherent phonons during the photoinduced insulator-to-metal phase transition in neodymium nickelate

Oleg Dogadov,[1,*,†] Grace A. Pan,[2,‡] Andrea Villa,[1] Dan Ferenc Segedin,[2] Premysl Marsik,[3]
Charles M. Brooks,[2] Hanjong Paik,[4,§] Qi Song,[2,‖] Valeria Russo,[5] Carlo S. Casari,[5] Julia A. Mundy,[2,6]
Giulio Cerullo,[1,7] and Stefano Dal Conte[1,¶]

[1]*Department of Physics, Politecnico di Milano, Piazza Leonardo da Vinci 32, Milan 20133, Italy*
[2]*Department of Physics, Harvard University, Cambridge, Massachusetts 02138, USA*
[3]*Department of Physics, University of Fribourg, Fribourg, Switzerland*
[4]*Platform for the Accelerated Realization, Analysis, and Discovery of Interface Materials (PARADIM), Cornell University, Ithaca, New York 14853, USA*
[5]*Department of Energy, Politecnico di Milano, Via Lambruschini, Milan 20156, Italy*
[6]*School of Engineering and Applied Science, Harvard University, Cambridge, Massachusetts 02138, USA*
[7]*CNR-IFN, Piazza Leonardo da Vinci 32, Milan 20133, Italy*

(Received 24 July 2025; revised 6 November 2025; accepted 1 December 2025; published 9 January 2026)

The interplay between electronic and lattice degrees of freedom in the insulator-to-metal transition (IMT) in rare-earth nickelates is a long-standing question. In the present work, broadband ultrafast transient reflectivity (TR) spectroscopy is applied to study the photoinduced IMT in $NdNiO_3$. Both coherent and incoherent terms of the TR signal show discontinuous behavior around the same pump fluence value. A drastic drop in the sample reflectivity appearing at ~100 fs timescale in the high excitation density regime indicates the closing of the gap across the IMT. In this regime, coherent phonons associated with the low-temperature crystal phase are not observed even at early time delays, indicating an ultrafast transformation of the lattice potential. A detailed analysis of the coherent phonons indicates a strong coupling between some phonon modes, electronic excitations, and possibly the magnetic order. In this study, we provide insights into the ultrafast dynamics of rare-earth nickelates.

DOI: 10.1103/yg97-vfmn

I. INTRODUCTION

Rare-earth perovskite nickelates with the chemical formula $R\mathrm{NiO}_3$, where R is a rare-earth element, represent a family of materials exhibiting rich physics [1,2]. All materials with $R \neq \mathrm{La}$ display an insulator-to-metal transition (IMT) [3], which in the case of Pr or Nd is also accompanied by the loss of long-range antiferromagnetic order [4]. From the time of its discovery, the nature of the IMT and insulating phase has been a matter of debate [5–11]. It was found that the transition from high-temperature metallic to low-temperature insulating phase is accompanied by a structural phase transition from orthorhombic *Pbnm* to monoclinic $P2_1/n$ phase [12,13]. It was predicted that a breathing distortion leading to bond disproportionation with long and short Ni–O bonds, creating compressed and expanded arrangements of NiO_6 octahedra [14], plays a key role in the stabilization of the insulating state in $R\mathrm{NiO}_3$ [see the $NdNiO_3$ low-temperature crystalline structure in Fig. 1(a)] [5,10,15,16]. The breathing distortions are found to be accompanied by the formation of a charge-ordered state [17], which according to current agreement is related to a self-doping effect resulting in a separation of ligand holes [5,15,18].

Since the observation of distinct electronic dynamics of insulating and metallic phases in $NdNiO_3$ [19], different out-of-equilibrium techniques were applied to establish the role of different degrees of freedom in the IMT [20–22]. A strong connection between the melting of the charge order and the electronic phase transition was revealed by combining time-resolved resonant x-ray diffraction and optical transient reflectivity (TR) spectroscopies [21]. In a recent study by Stoica *et al.* [22], the dynamics of magnetic, electronic, and structural phase transition in $NdNiO_3$ was investigated by combined transient x-ray and terahertz (THz) techniques. The reported results indicated that the melting of the magnetic order precedes the electronic and structural changes appearing a few hundred femtoseconds after the photoexcitation.

---

[*] Contact author: oleg.dogadov@polimi.it

[†] Present address: Department of Physical Chemistry, Fritz Haber Institute of the Max Planck Society, 14195 Berlin, Germany.

[‡] Present address: Department of Physics, University of California, Berkeley, California, USA.

[§] Present address: School of Electrical and Computer Engineering, University of Oklahoma, Norman, Oklahoma, USA.

[‖] Present address: Department of Materials Science and Engineering, University of California, Irvine, California, USA.

[¶] Contact author: stefano.dalconte@polimi.it

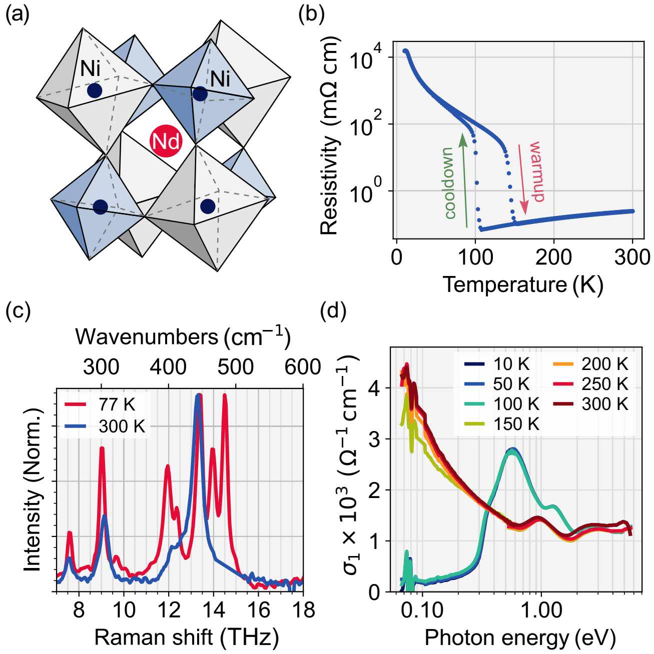

FIG. 1. (a) Sketch of the low-temperature monoclinic crystalline structure of $NdNiO_3$, illustrating compressed (blue) and expanded (gray) octahedral arrangements of nickel sites. (b) Electrical resistivity temperature dependence for the studied $NdNiO_3$ crystalline film. The data shown here were previously reported in Ref. [23], in which the sample studied in our work was characterized. (c) Raman spectra for the two crystalline phases of $NdNiO_3$ measured at 77 and 300 K. (d) Temperature dependence (warmup) of the real part of the optical conductivity of the $NdNiO_3$ film obtained by point-by-point fits to the ellipsometry data in broad spectral range.

Despite extensive studies performed over the last few years on rare-earth nickelates, a complete picture describing the role of different degrees of freedom in the IMT in these materials remains elusive, and more experimental and theoretical studies are required to build a coherent picture.

In this work, we apply broadband optical TR spectroscopy with high temporal resolution (i.e., ~30 fs) to monitor both the changes in the electronic response and the evolution of the coherent phonons in photoexcited $NdNiO_3$ across the IMT. We find that high-frequency phonon modes involving distortions of NiO_6 octahedra are particularly sensitive to the photoexcitation. For strong laser excitation, we observe a dramatic decrease of the reflectivity within approximately 100 fs, followed by the formation of a long-lived signal, indicating a transition to the metastable metallic state. At the same time, the coherent phonons of the low-temperature phase are not present in the TR traces in the strong excitation regime even at early time delays. In this study, we demonstrate that the electronic IMT and ultrafast lattice modifications are strongly connected in $NdNiO_3$, providing important information for future studies of rare-earth nickelates and their heterostructures.

II. NEODYMIUM NICKELATE THIN FILM

$NdNiO_3$ thin film has been synthesized on a $LaAlO_3$ substrate using reactive oxide molecular beam epitaxy at 550 °C. The details of the fabrication and sample characterization with x-ray absorption and diffraction techniques are reported in Ref. [23]. The thickness of the film is 22.9 nm. Basic electrical characterization is performed in the van der Pauw geometry in a Physical Property Measurement System using standard AC lock-in techniques at ~15 Hz. Resistivity measurement shown in Fig. 1(b) presents a sharp IMT. The cooldown and warmup transition temperatures determined from the reported measurements are around 108 and 150 K, respectively, like in previous works [17,23]. Such hysteretic behavior is due the phase coexistence close to the IMT temperature, which is expected for a first-order phase transition. A broad hysteresis loop is commonly observed in electrical resistivity measurements for $NdNiO_3$, for which it has been extensively investigated [24–29], and for $PrNiO_3$ [30], whereas it is less prominent for the nickelates with smaller rare-earth cations [29,31]. The IMT temperature is slightly lower than in bulk $NdNiO_3$ [1,3] due to $\varepsilon \simeq -0.4\%$ compressive strain [23], induced by the $LaAlO_3$ substrate [32–34]. Additional sample characterization, performed in this work, confirms the IMT in the studied sample: Raman scattering measurements, reported in Fig. 1(c), reveal distinct phonon modes at 77 and 300 K, in agreement with previously reported studies on $NdNiO_3$ [35–37], confirming the change of the crystal symmetry across the IMT. Figure 1(d) shows temperature dependence of the real part of optical conductivity of the $NdNiO_3$ film, extracted from ellipsometry measurements with an ambient/film/substrate model. The spectra reveal the presence of several overlapping features from the midinfrared (mid-IR) to ultraviolet range, assigned to transitions between lower-Hubbard-band and oxygen orbitals to unoccupied states [38–40]. Narrow peaks in the far-IR part of the spectra are due to IR-active phonon modes of $NdNiO_3$ and the substrate (see also Fig. S2 in the Supplemental Material (SM) [41]). Below 150 K, the sample has a band gap of around 300 meV, while at higher temperature, the metallic phase is characterized by a rise of a Drude peak. The details on spontaneous Raman scattering and steady-state ellipsometry measurements are provided in the SM [41].

III. NONEQUILIBRIUM RESPONSE TO A WEAK PERTURBATION

TR measurements are performed on the $NdNiO_3$ film at 2 kHz repetition rate. In our experiment, the sample is excited by a pump pulse with ~30 fs duration centered at 2.4 eV. The changes of the reflectivity are monitored in the 1.7–2.3 eV range by a delayed broadband probe pulse. We first discuss measurements performed in a weakly perturbative regime, in which the pump fluence of 60 μJ cm^{-2} is used to prevent strong perturbation of the system (see fluence dependence in Sec. IV). Further experimental details are provided in the SM [41].

The experimental results of the TR measurements for the two adiabatic phases of $NdNiO_3$ are summarized in Fig. 2. Figures 2(a) and 2(e) show pseudocolor $\Delta R/R$ maps for the insulating (77 K) and metallic (300 K) states, respectively. In the low-temperature insulating phase, the reflectivity of the sample immediately after the photoexcitation is quenched in the two electronic bands with the energies below 1.8 eV

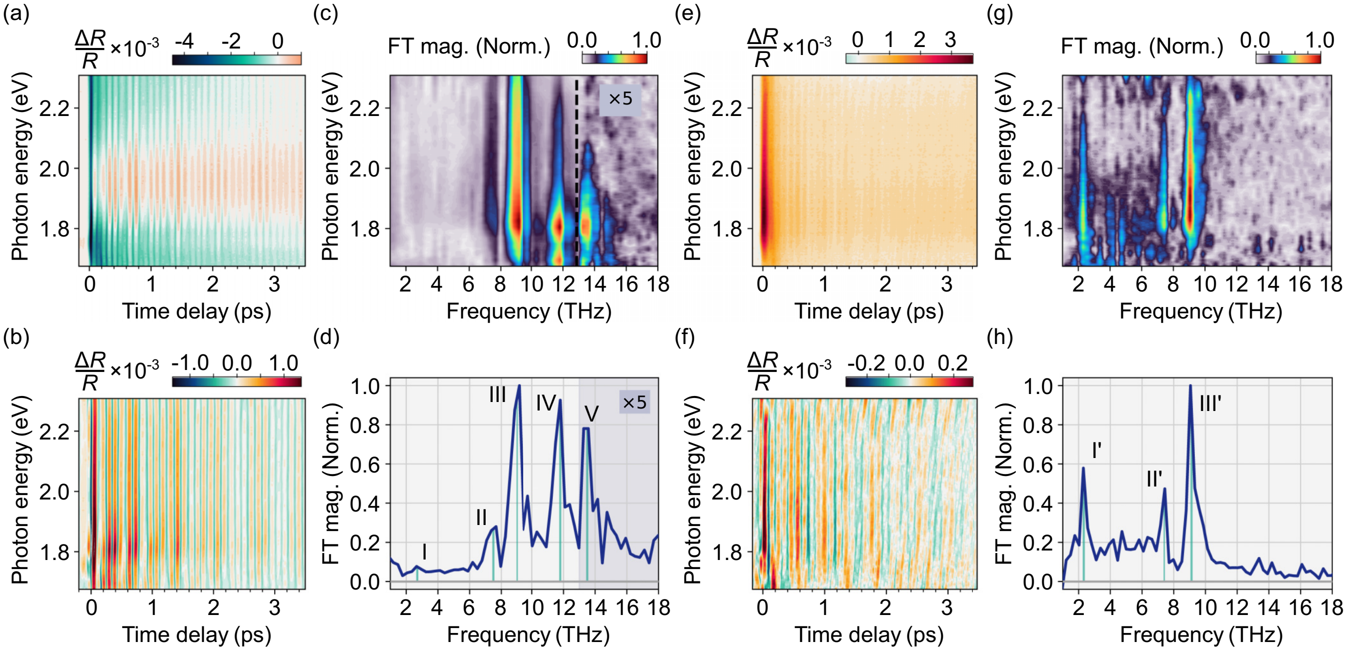

FIG. 2. Transient response of $NdNiO_3$ to a weak perturbation at (a)–(d) 77 K and (e)–(h) 300 K. (a) and (e) Pseudocolor TR maps. (b) and (f) Oscillatory components of the transient signals. (c) and (g) FT maps of the maps (b) and (f), respectively. (d) and (h) FT spectra at 1.82 eV probe energy.

and above 2.1 eV, resulting in negative $\Delta R/R$. The shape of the transient signal is consistent with the ellipsometry measurements shown in Fig. 1(d) and in Fig. S2 in the SM [41] as well as with the reported studies on $NdNiO_3$ electronic structure [38,39]. The initial negative $\Delta R/R$ signal recovers with time constants of $\sim$0.4 ps and 3 ps (see fit in Fig. S5 in the SM [41]). Above the transition temperature, i.e., in the metallic state, the differential signal is positive and almost featureless in the whole probe range, as shown in Fig. 2(e). The TR of the high-temperature metallic phase displays an instantaneous rise, i.e., limited by the instrument response function, followed by a fast decay and a plateau with relaxation times $\tau_1 \simeq 120$ fs and $\tau_2 \gtrsim 20$ ps. Such behavior is typical for metallic systems, and the two components are generally attributed to the electron-phonon thermalization and the heating of the lattice, respectively [42,43].

In both phases, the transient signal is significantly modulated by coherent oscillations [44] across the whole spectrum. The intensity of the oscillations is enhanced around 1.8 eV, indicating an increased coupling strength to the interband transitions in that energy range [45–47], although the microscopic origin of the associated states is under debate [39,40]. The oscillatory component of the signals, retrieved from the experimental maps by subtracting global fit maps of the incoherent part [48], is shown in Figs. 2(b) and 2(f) for the insulating and metallic phases, respectively. (See details in the SM [41].) The Fourier transform (FT) maps reported in Figs. 2(c) and 2(g) reveal the presence of multiple phonon modes, modulating the TR signal. The strongest modes at 77 K are observed at 7.5 THz [250 cm^{-1}, labeled as Mode II, as shown in Fig. 2(d), displaying FT at 1.82 eV probe energy], 9.0 THz (300 cm^{-1}, Mode III), and 11.8 THz (394 cm^{-1}, Mode IV), although other lower intensity oscillations are also present in the FT, such as Mode I at 2.6 THz (87 cm^{-1}), Mode V at $\sim$13.5 THz (450 cm^{-1}), and an additional peak at 9.6 THz (320 cm^{-1}).

In the high-symmetry (metallic) phase, the coherent phonon mode content is different, as shown in Figs. 2(g) and 2(h). A low-frequency mode, almost indistinguishable at low temperature, is clearly seen at 2.3 THz (76 cm^{-1}, Mode I′). The doublet at 9.0 and 9.6 THz, observed in the insulating phase, collapses into a single peak around 9.2 THz (307 cm^{-1}, Mode III′). Mode II$^{(\prime)}$ remains almost unchanged, showing a minor hardening in the high-temperature phase.

The phonon modes revealed in the FT for both crystal phases match the peaks observed in Raman scattering measurements reported in Fig. 1(c) well (see also Fig. S1 in the SM [41]). The coherent responses of the two crystal phases can therefore be clearly distinguished with the precision of our TR measurements. Importantly, no coherent oscillations are observed in the metallic phase for the frequencies above 10 THz, although they are present in the static Raman spectra [see Fig. 1(c)], which is critical for the analysis reported in Sec. V, in which the changes in the coherent phonons with temperature and pump fluence are discussed. The absence of the coherent modes above 10 THz can either be due to the low symmetry of the phonons in that frequency range [35] or due to their reduced coupling with the probed electronic states [49]. We also note that no coherent phonon signal from the substrate is observed in our measurements, as shown in Fig. 10 in the SM [41]. In the following section, we discuss how the transient response of the material evolves with increasing pump fluence.

IV. FLUENCE DEPENDENCE

To explore the effect of excitation density on the optical properties of $NdNiO_3$, we perform pump-fluence-dependent

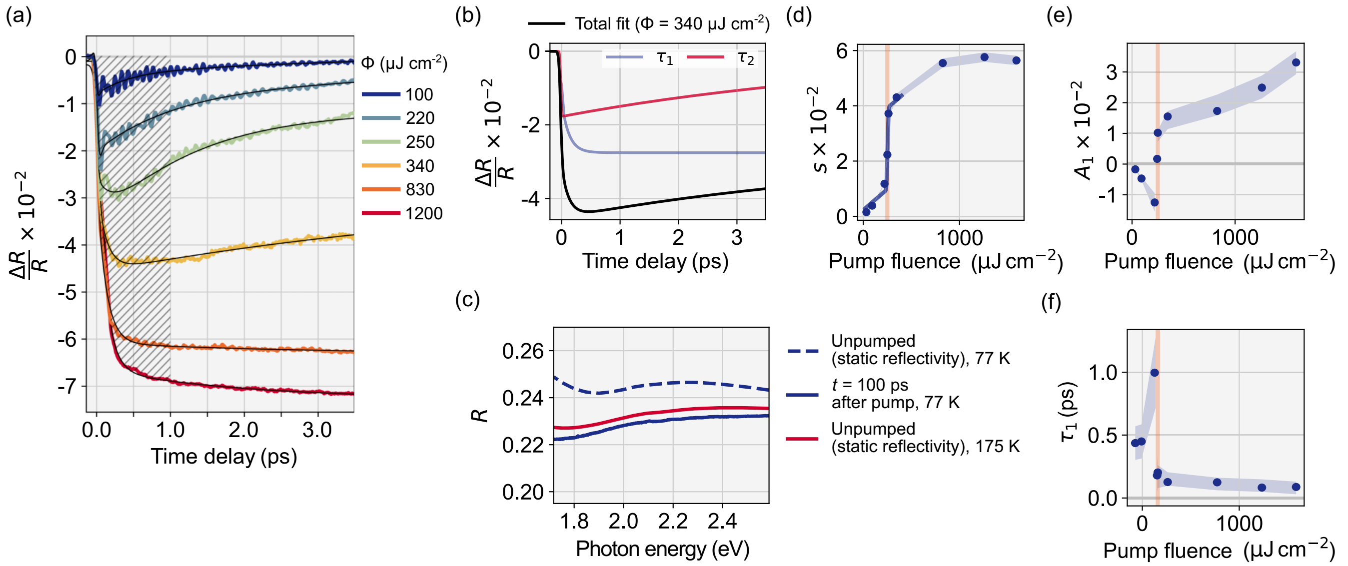

FIG. 3. Fluence dependence. (a) TR traces at 1.82 eV probe energy for select pump fluences. Thin black lines show the fit with Eq. (3). (b) Total fit and two exponential components from Eq. (3) with the τ_1 component showing delayed rise above critical fluence [$\Phi = 1.4\,\Phi^*$, yellow trace in panel (a)]. (c) Nonequilibrium reflectivity measured at $t = 100$ ps for $\Phi = 4.4\,\Phi^*$ at 77 K (solid blue line) approaching static reflectivity above the transition temperature (dashed blue line). (d) Integral of the transient signal calculated as in Eq. (1) over the hatched area shown in panel (a). Solid line shows the fit with the function in Eq. (2). Fluence dependence of the fit parameters (e) A_1 and (f) τ_1, determined from Eq. (3). Vertical orange lines in (d)–(f) indicate the fluence Φ^*; the error bars are represented by the thickness of the filled areas.

measurements, like in previous works on systems with strong electron-phonon coupling [50–52]. In these measurements, the sample is kept at 77 K (i.e., in the insulating phase), and the pump fluence is varied over more than an order of magnitude from tens of μJ cm^{-2} to more than 1 mJ cm^{-2}. To achieve homogeneous excitation over the probe beam profile, the pump beam spot size on the sample surface has been set to be at least two times larger than that of the probe beam. Because of the qualitative similarity of the transient signal for different probe photon energies (see also Fig. S7 in the SM [41]), we focus here on the probe region around 1.8 eV, where the overall signal is negative, and the coherent signal is enhanced.

The transient traces at 1.82 eV for select excitation densities are reported in Fig. 3(a). As the pump fluence increases, the signal becomes qualitatively different from that discussed before (see, e.g., the yellow trace, corresponding to 340 μJ cm^{-2}): after the excitation, the TR continues to decrease within a few hundreds of femtoseconds and then recovers at a much slower rate. For higher fluences, after the initial delayed formation, the reflectivity keeps decreasing on a picosecond timescale up to the longest experimentally explored time delay of 100 ps (see Fig. S7 in SM [41]), like in previous studies [21,53,54]. We note, however, that the transition is fully reversible up to the highest explored pump fluence of 1.6 mJ cm^{-2}, and the recovery time is significantly shorter than 0.5 ms time distance between consecutive probe pulses. The reflectivity drop upon photoexcitation with high pump fluences is consistent with lower reflectivity of the metallic state, as shown in the static reflectivity data, extracted from the ellipsometry results, depicted in Fig. 3(c) and Fig. S2 in the SM [41]. The reflectivity is calculated with the transfer matrix method (TMM) [55] for the system vacuum/NdNiO$_3$ film/LaAlO$_3$ substrate [56]. The static reflectivity in the metallic state and the nonequilibrium reflectivity in the photoexcited state show a similar shape with a vanishing low-energy peak. The discrepancy between the two spectra can be because the applied TMM model does not consider the light that is backscattered from the opaque rear surface of the substrate, which is in contact with the cold finger of the cryostat. The observed drastic changes in the reflectivity of NdNiO$_3$ indicate a significant modification of the electronic structure of the system upon photoexcitation and the formation of a metastable state.

To quantify the effect of the increasing pump fluence Φ on the response of the system, we explore the evolution of the signal intensity as a function of Φ. Figure 3(d) reports the integral $s(\Phi)$ of the transient signal at 1.8 eV over the first picosecond after the photoexcitation as a function of incident pump fluence:

$$s(\Phi) = -\int_0^{1\,\mathrm{ps}} dt\, \frac{\Delta R}{R}(\Phi, t). \tag{1}$$

The region of integration is indicated with a shaded area in Fig. 3(a). In a narrow range of fluences, the signal experiences a dramatic change, which strongly deviates from the behavior at low fluences. We estimate the threshold value of Φ^*, at which the signal experiences such changes, by fitting $s(\Phi)$ with a function

$$s(\Phi) = A\left[1 - \mathrm{erf}\left(\frac{\Phi - \Phi^*}{\delta\Phi}\right)\right] + b\,\Phi. \tag{2}$$

Here, erf is the Gauss error function, considering the discontinuous component, and the linear term includes the linear growth of the signal with the incident fluence at the low-fluence regime. The fit is shown in Fig. 3(d) with a solid line. The estimated value of the critical fluence $\Phi^* \simeq 250$ μJ cm^{-2} is marked in the figure with a vertical orange line. The determined value of Φ^* corresponds to the excitation of one site in about 130 unit cells, considering the unit cell volume 55 Å^3 [23] and estimating from the performed ellipsometry measurements the absorption of a 22.9 nm film at 2.3 eV to be of $\sim$0.5. From the volumetric heat capacity of $NdNiO_3$ at 77 K being around 1.5 J cm^{-3} K^{-1} [57,58] and the calculated absorption, we also estimate the transient heating of the sample per pulse for this fluence to not exceed $\Delta T = 30$ K, which is much lower than the difference between the sample temperature and the phase transition temperature $T^* \simeq 150$ K, confirming that the observed transition is not due to the transient heating of the sample. The found threshold fluence Φ^* in $NdNiO_3$ is on the same order of magnitude as previously reported for $NdNiO_3$ on $NdGaO_3$ substrate [21] and for $SmNiO_3$ on $LaAlO_3$ [59], and it is much lower than the values reported for other IMT materials, such as VO_2 [60], V_2O_3 [50], or $La_{0.5}Sr_{1.5}MnO_4$ [61], which are typically on the order of several μJ cm^2.

We further explore the evolution of the incoherent part of the signal with the pump fluence by fitting the TR traces with a two-exponential function, convoluted with a single Gaussian $\mathcal{G}(\sigma, t)$, representing the IRF

$$\frac{\Delta R}{R}(t) = H(t - t_0)\left[\sum_{i=1}^{2} A_i \exp\left(-\frac{t - t_0}{\tau_i}\right) + a\right] * \mathcal{G}(\sigma, t). \tag{3}$$

Here, $H(t - t_0)$ is the Heaviside step function. The fit traces are shown in Fig. 3(a) with thin black lines. Figures 3(e) and 3(f) report the amplitude A_1 and the time constant τ_1 of the fast exponential component. Blue filled areas represent the errors of the fit. Both parameters show a discontinuous behavior around the threshold fluence Φ^*, marked with a vertical orange line, indicating drastic changes in the electronic response of the sample. The amplitude of the exponent A_1 changes the sign from negative to positive, as it crosses Φ^*, meaning that, for the fluences exceeding Φ^*, the formation of the transient signal is delayed. The delayed formation of the TR signal, associated with the first exponential component is shown in Fig. 3(b) for $\Phi = 1.4\,\Phi^*$. This delay can be associated with the formation of a metastable metallic state upon the closure of the gap, which is accompanied by a spectral weight transfer from high-energy states to the Drude peak, consistent with the reflectivity changes shown in Fig. 3(c).

Additionally, we have explored the effect of the pump photon energy on the dynamics of photoinduced phase transition. For this, similar measurements have been performed using a two-color TR technique with mid-IR excitation at $\sim$440 meV, i.e., close to the band gap. However, only marginal differences between the two excitation regimes have been observed, as shown in Fig. S9 in the SM [41], indicating the similarity of the mechanisms driving the IMT for the two excitation photon energies. We therefore focus on the results obtained for the excitation in the visible.

We have also performed fluence dependence measurements at 300 K, i.e., well above the phase transition temperature T^*. The results are reported in Fig. S6 in the SM [41]. For all explored fluences, the transient response of the system remains similar, confirming that the discontinuity observed in the TR measurements are present only in the low-temperature semiconducting phase and are associated with the photoinduced IMT.

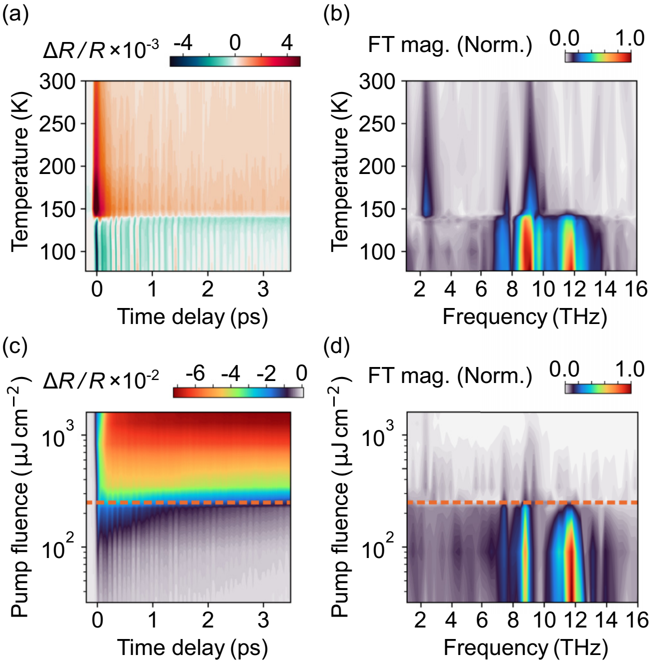

FIG. 4. Temperature and fluence dependence comparison. Evolution of TR at (a) 1.82 eV and (b) corresponding FT magnitudes for increasing sample temperature. Evolution of transient reflectivity at (c) 1.82 eV and (d) corresponding FT magnitudes for increasing pump fluence. Dashed horizontal lines in (c) and (d) mark threshold fluence $\Phi^* \simeq 250$ μJ cm^{-2} determined as explained in text.

V. FLUENCE AND TEMPERATURE DEPENDENCE OF THE COHERENT PHONONS

As discussed in Sec. III, in both low- and high-temperature phases the transient response of the system is modulated by coherent oscillations. We now discuss the evolution of the coherent phonons across the temperature- and photoinduced phase transitions. Figure 4(a) reports differential reflectivity traces at 1.82 eV probe photon energy for different sample temperatures. For these measurements, the sample is cooled down to 77 K, and the temperature dependence is acquired upon warming up. A relatively low fluence of around 140 μJ cm^{-2} ($\sim$0.56 Φ^*) has been chosen to prevent strong perturbation of the system, having at the same time higher signal-to-noise ratio. An abrupt change of the differential reflectivity signal sign is observed around $T^* = 143$ K, close to the warmup IMT temperature determined by steady-state sheet resistivity measurements [see Fig. 1(b)]. The temperature mismatch can be related to higher starting temperature in our TR temperature scan (77 K) than that in the resistivity measurements as well as the pump-induced transient heating of the sample. The corresponding FT spectra are shown in Fig. 4(b). Below and above the transition temperature, the FT spectra are characterized by the presence of phonon modes

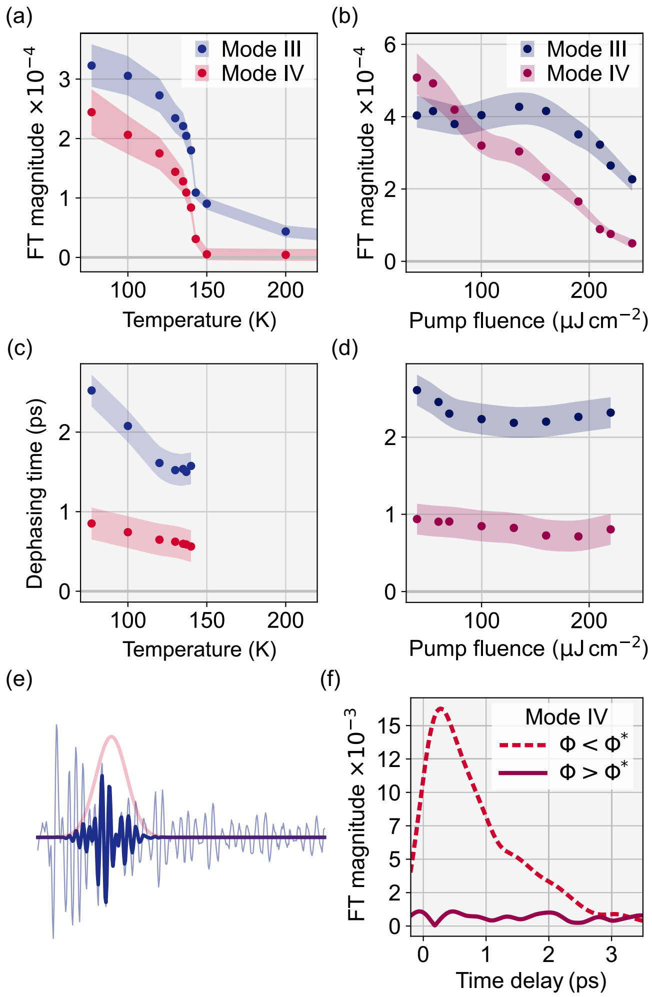

FIG. 5. Parameters of Modes III and IV, shown in blue and red, respectively. (a) Temperature and (b) fluence dependence of FT magnitudes, normalized to corresponding pump-fluence values. (c) Temperature and (d) fluence dependence of phonon dephasing time, determined by STFT analysis. The error bars are represented by the thickness of the filled areas. (e) Illustration of the STFT: sliding Gaussian time window $\mathcal{G}(\sigma, \mu)$ selects data range within which the mode content is explored. (f) STFT of Mode IV below ($\Phi = 0.12\,\Phi^*$) and above ($\Phi = 3.3\,\Phi^*$) threshold fluence ($T = 77$ K), showing that Mode IV is not present for $\Phi > \Phi^*$.

of low- and high-symmetry phases, respectively, described in Sec. III [see also Figs. 2(d) and 2(f)]. The decreasing phonon intensity at higher temperatures in the metallic phase can be related to a reduction of the optical conductivity [62].

Like the temperature dependence, Fig. 4(c) shows the evolution of the differential reflectivity signal for increasing pump fluences. In these measurements, the sample is kept at 77 K. The pump fluence (ordinate axis) is shown in logarithmic scale. As discussed in Sec. IV, for increasing pump fluences, the signal experiences drastic changes, such as the nonlinear signal intensity increase and the formation of the metastable metallic state. The map in Fig. 4(d) reports the corresponding FT coherent phonon spectra. All spectra are normalized to the pump fluences to remove the effects that depend linearly on the excitation density. Dashed horizontal lines in Figs. 4(c) and 4(d) indicate threshold fluence Φ^*. When the pump fluence exceeds Φ^*, the intense phonon peaks of the monoclinic phase disappear. Note that Φ^* has been determined from the incoherent (electronic) response of the system and has been associated with the change of the dynamics character from a decay to a delayed rise. The analysis of the coherent phonons indicate that the photoinduced IMT is accompanied by significant modification of the lattice potential. The weak peaks observed in the FT map above the threshold fluence are likely related to the incomplete phase transition in the probed volume for moderate pump fluences or to the coherent response of the orthorhombic phase fraction, which can be present below the transition temperature [63–65].

Despite major similarities in the FT spectra for the laser-driven IMT below the threshold fluence and the temperature-induced IMT below the transition temperature, there are some notable differences. Figures 5(a)–5(d) compare parameters of the two most intense modes, i.e., Modes III and IV. Figure 5(a) shows the evolution of the FT magnitudes with temperature, extracted from the map in Fig. 4(b). For increasing temperatures, the intensity of both modes progressively diminishes and sharply drops as the temperature approaches T^*, as expected for a first-order phase transition. The intensity of Mode IV shows a stronger dependence on the sample temperature, as previously shown in Raman scattering measurements [35]. The nonzero signal above T^* for the blue trace is due to Mode III$'$ of the high-temperature orthorhombic phase, which has a very similar frequency (9.2 THz). Conversely, the pump-fluence dependence of the two modes is qualitatively different: Whereas the intensity of Mode III is almost constant up to ∼160 μJ cm^{-2} within the error of the measurement and drops as the fluence approaches Φ^*, resembling the temperature dependence, Mode IV intensity shows a gradual decrease over the whole fluence range below Φ^*. A similar analysis performed for Mode II (see SM [41]) shows that such behavior is unique for Mode IV.

Together with the FT magnitude of the phonon modes as a function of temperature and fluence, we retrieve information about the phonon dynamics via a short-time FT (STFT) analysis [66]. In this method, the frequency content of the oscillating component of a TR signal is examined within a moving Gaussian window $\mathcal{G}(\sigma_t, t-\mu)$, where μ is varying position of the window

$$\mathcal{F}_{\mathrm{ST}}(\mu, \omega) = \int_{-\infty}^{+\infty} dt \left.\frac{\Delta R(t)}{R}\right|_{\mathrm{osc}} \mathcal{G}(\sigma_t, t-\mu)\exp(-i\omega t). \tag{4}$$

Figure 5(e) illustrates a wavelet selected by a window $\mathcal{G}(\sigma_t, t-\mu)$. For the Gaussian window, $\sigma_t = 250$ fs gives the frequency uncertainty $\sigma_f = 2$ THz, allowing us to track the dynamics of Modes III and IV independently. The resulting three-dimensional matrix in Eq. (4) contains information about the temporal evolution of the FT of the coherent signal for all probe photon energies. In principle, the information about the phonon dephasing can also be obtained by performing an approximation of the transient traces with a combination of exponential decays and damped cosine functions (see, e.g., Eq. (2) in the SM [41]). However, such an analysis is complicated because of the high number of strong coherent modes as well as the increased noise as the pump fluence approaches Φ^*.

The phonon dephasing times are extracted from STFT traces around 9.0 THz (for Mode III) and 11.8 THz (for Mode IV) calculated for 1.82 eV probe photon energy, assuming a monoexponential decay law. A typical trace is shown in Fig. 5(f). The results of the phonon lifetime analysis are summarized in Figs. 5(c) and 5(d). For increasing sample temperatures, a stronger damping is observed for both modes, which can be explained by a larger probability of phonon-phonon scattering at higher temperatures [67]. For all temperatures, the dephasing rate of Mode IV is roughly two times higher than that of Mode III. In contrast, the phonon dephasing time does not seem to be affected significantly by the pump fluence, as shown in Fig. 5(d). The observed fluence dependence of the phonon intensity is not related, therefore, to a faster coherent phonon dephasing.

We further apply the STFT to explore the evolution of the coherent phonons in the photoexcited s$NdNiO_3$ when the pump fluence exceeds Φ^*. Figure 5(f) compares intensity profiles of Mode IV for two pump fluences below ($\sim$30 μJ cm^{-2} = 0.12Φ^*) and above ($\sim$830 μJ cm^{-2} = 3.3Φ^*) the IMT threshold. The traces are extracted from the STFT maps at 1.82 eV for the frequency region around 11.8 THz. For low pump fluence, the phonon intensity profile shows a finite formation time defined by σ_t of the Gaussian window and a decay of ~1 ps. When the pump fluence exceeds Φ^*, no considerable signature of Mode IV, which is present only in the low-temperature monoclinic phase, is observed even at early time delays.

VI. DISCUSSION AND CONCLUSIONS

The fluence dependence of the TR in $NdNiO_3$ shows a sharp discontinuity in the parameters of both the coherent and incoherent components of the signal around the threshold fluence $\Phi^* \simeq 250$ μJ cm^{-2}. For pump fluences exceeding Φ^*, the TR signal has a delayed rise with a characteristic time of ~100 fs. The observed delayed formation of the signal indicates that a strong pump induces a significant modification of the sample reflectivity due to the photoinduced closure of the gap and the consequential spectral weight transfer. The observed timescale can be defined by different factors affecting the photoresponse of the system, depending on the driving force of the phase transition. For instance, it can be related to the carrier thermalization [68], required for the reconstruction of the carrier distribution in the metallic phase upon closing of the gap, or to a phonon bottleneck [69], in case a structural change is the driving force of the IMT. The long rise-time component appearing on a picosecond timescale (see also Fig. S7 in the SM [41]) in the TR traces for $\Phi \gg \Phi^*$, i.e., when the the probed volume is homogeneously excited, can be related to the sample cooling [54] or to relatively slow structural modifications in the photoinduced phase [70,71].

When the pump fluence exceeds Φ^*, the coherent phonons of the low-temperature monoclinic phase promptly disappear upon photoexcitation. As shown in Fig. 5(f), Mode IV is not observed in the high-fluence regime even at early time delays, indicating an ultrafast change of the lattice potential accompanying the IMT.

It has recently been reported that an ultrafast quench of the magnetic order precedes the electronic and structural transition in $NdNiO_3$, both appearing at approximately 450 fs after the optical pumping [22]. Moreover, the Nd magnetic scattering signal is modulated by a low-frequency phonon mode—matching Mode I in the present work—even at pump fluences exceeding the IMT threshold. Our findings suggest that such a description is not complete. The lifetime analysis shows that, above Φ^*, the electronic response of the system is significantly modified within the first ~100 fs, and the high-frequency phonon modes are not observed even at early time delays. These results suggest that ultrafast lattice potential transformations are linked to the electronic modifications, and they play an important role in the photoinduced IMT in rare-earth nickelates.

The detailed analysis of the pump-fluence dependence shows that some phonon modes are significantly affected by the laser excitation. The intensity of Mode IV decreases gradually with increasing photocarrier density, indicating a strong modification of particular electron states involved in the corresponding motion by the generated carriers. The high-frequency phonons present in the low-temperature monoclinic phase in $NdNiO_3$ are related to the distortions of oxygen octahedra [16,35,72] and are therefore particularly sensitive to the changes in the parameters of Ni–O bonding. It should be noted that the low-temperature insulating phase is antiferromagnetic, and the antiferromagnetic order is believed to play an important role in the stabilization of the insulating phase [73]. Raman scattering studies on rare-earth nickelates have reported significant changes in the parameters of high-frequency phonon modes above the Néel temperature [36,37], indicating a possible spin-phonon coupling, which may affect the observed phonon parameters [74,75]. We also note that the fluence dependence of the Ni magnetic scattering reported in Ref. [22] shows a similar trend to that of Mode IV in Fig. 5(b). For a correct description of the coherent phonon dynamics, it may therefore be necessary to consider the evolution of both the electronic and magnetic systems upon photoexcitaton.

In conclusion, the reported all-optical TR measurements have revealed the photoinduced IMT in a thin film of neodymium nickelate. Both coherent and incoherent parts of the signal change within approximately 100 fs upon photoexcitation above the threshold fluence, indicating a simultaneous electronic phase transition and a strong modification of lattice potential. A detailed investigation of coherent phonons has unveiled anomalous behavior of a high-frequency mode involving the oxygen octahedra distortion, indicating its link to the phase transition. These findings suggest that ultrafast lattice transformations play an important role in the photoinduced IMT in nickelates.

ACKNOWLEDGMENTS

The authors thank C. J. Sayers and A. Crepaldi for helpful discussions and acknowledge A. Iudica and L. Brambilla for their assistance with the experiments. O.D. and G.C. acknowledge financial support from the European Union's NextGenerationEU Programme with the project PRIN PNRR 2022 [ID P20224AWLB, CUP D53D23016720001]. Thin film synthesis was supported by the U.S. Department of

Energy, Office of Basic Energy Sciences, Division of Materials Sciences and Engineering, under Award No. DE-SC0021925. In this work, we made use of the synthesis facilities of the PARADIM, which is supported by the National Science Foundation (NSF) under Cooperative Agreement No. DMR-2039380. G.A.P. and D.F.S. are supported primarily by the NSF Graduate Research Fellowship Grant No. DGE-1745303. G.A.P. acknowledges additional support from the Paul & Daisy Soros Fellowship for New Americans. J.A.M. acknowledges support from the Packard Foundation and Gordon and Betty Moore Foundation's EPiQS Initiative (Grant No. GBMF6760). Q.S. was supported by the Science and Technology Center for Integrated Quantum Materials, NSF Grant No. DMR-1231319. S.D.C and G.C. acknowledge financial support by the European Union's NextGenerationEU Programme with the I-PHOQS Infrastructure [IR0000016, ID D2B8D520, CUP B53C22001750006] "Integrated infrastructure initiative in Photonic and Quantum Sciences". S.D.C. acknowledges support from the European Union's NextGenerationEU Investment 1.1, M4C2 - Project n. 2022LA3TJ8 CUP D53D23002280006. P.M. acknowledges support from the Swiss National Science Foundation (SNSF) by Grant No. 200021-231685.

DATA AVAILABILITY

The data that support the findings of this article are openly available [76].

---

[1] M. L. Medarde, Structural, magnetic and electronic properties of RNiO$_3$ perovskites (R = rare earth), J. Phys.: Condens. Matter **9**, 1679 (1997).

[2] S. Catalano, M. Gibert, J. Fowlie, J. Íñiguez, J.-M. Triscone, and J. Kreisel, Rare-earth nickelates RNiO$_3$: Thin films and heterostructures, Rep. Prog. Phys. **81**, 046501 (2018).

[3] P. Lacorre, J. Torrance, J. Pannetier, A. Nazzal, P. Wang, and T. Huang, Synthesis, crystal structure, and properties of metallic PrNiO$_3$: Comparison with metallic NdNiO$_3$ and semiconducting SmNiO$_3$, J. Solid State Chem. **91**, 225 (1991).

[4] J. L. García-Muñoz, J. Rodríguez-Carvajal, and P. Lacorre, Sudden appearance of an unusual spin density wave at the metal-insulator transition in the perovskites RNiO$_3$ (R = Pr, Nd), Europhys. Lett. **20**, 241 (1992).

[5] H. Park, A. J. Millis, and C. A. Marianetti, Site-selective Mott transition in rare-earth-element nickelates, Phys. Rev. Lett. **109**, 156402 (2012).

[6] A. Subedi, O. E. Peil, and A. Georges, Low-energy description of the metal-insulator transition in the rare-earth nickelates, Phys. Rev. B **91**, 075128 (2015).

[7] J. Varignon, M. N. Grisolia, J. Íñiguez, A. Barthélémy, and M. Bibes, Complete phase diagram of rare-earth nickelates from first-principles, npj Quantum Mater. **2**, 21 (2017).

[8] G. G. Guzmán-Verri, R. T. Brierley, and P. B. Littlewood, Cooperative elastic fluctuations provide tuning of the metal-insulator transition, Nature (London) **576**, 429 (2019).

[9] O. E. Peil, A. Hampel, C. Ederer, and A. Georges, Mechanism and control parameters of the coupled structural and metal-insulator transition in nickelates, Phys. Rev. B **99**, 245127 (2019).

[10] A. B. Georgescu and A. J. Millis, Quantifying the role of the lattice in metal-insulator phase transitions, Commun. Phys. **5**, 135 (2022).

[11] A. S. Moskvin, Insulator–bad metal transition in RNiO$_3$ nickelates beyond the Hubbard model and density functional theory, JETP Lett. **121**, 411 (2025).

[12] J. A. Alonso, J. L. García-Muñoz, M. T. Fernández-Díaz, M. A. G. Aranda, M. J. Martínez-Lope, and M. T. Casais, Charge disproportionation in RNiO$_3$ perovskites: Simultaneous metal-insulator and structural transition in YNiO$_3$, Phys. Rev. Lett. **82**, 3871 (1999).

[13] J. A. Alonso, M. J. Martínez-Lope, M. T. Casais, J. L. García-Muñoz, and M. T. Fernández-Díaz, Room-temperature monoclinic distortion due to charge disproportionation in RNiO$_3$ perovskites with small rare-earth cations (R = Ho, Y, Er, Tm, Yb, and Lu): A neutron diffraction study, Phys. Rev. B **61**, 1756 (2000).

[14] R. J. Green, M. W. Haverkort, and G. A. Sawatzky, Bond disproportionation and dynamical charge fluctuations in the perovskite rare-earth nickelates, Phys. Rev. B **94**, 195127 (2016).

[15] S. Johnston, A. Mukherjee, I. Elfimov, M. Berciu, and G. A. Sawatzky, Charge disproportionation without charge transfer in the rare-earth-element nickelates as a possible mechanism for the metal-insulator transition, Phys. Rev. Lett. **112**, 106404 (2014).

[16] A. Mercy, J. Bieder, J. Íñiguez, and P. Ghosez, Structurally triggered metal-insulator transition in rare-earth nickelates, Nat. Commun. **8**, 1677 (2017).

[17] J. L. García-Muñoz, M. A. G. Aranda, J. A. Alonso, and M. J. Martínez-Lope, Structure and charge order in the antiferromagnetic band-insulating phase of NdNiO$_3$, Phys. Rev. B **79**, 134432 (2009).

[18] T. Mizokawa, D. I. Khomskii, and G. A. Sawatzky, Spin and charge ordering in self-doped Mott insulators, Phys. Rev. B **61**, 11263 (2000).

[19] P. Ruello, S. Zhang, P. Laffez, B. Perrin, and V. Gusev, Ultrafast electronic dynamics in the metal-insulator transition compound NdNiO$_3$, Phys. Rev. B **76**, 165107 (2007).

[20] A. D. Caviglia *et al.*, Photoinduced melting of magnetic order in the correlated electron insulator NdNiO$_3$, Phys. Rev. B **88**, 220401(R) (2013).

[21] V. Esposito *et al.*, Dynamics of the photoinduced insulator-to-metal transition in a nickelate film, Struct. Dyn. **5**, 064501 (2018).

[22] V. A. Stoica, D. Puggioni, J. Zhang, R. Singla, G. L. Dakovski, G. Coslovich, M. H. Seaberg, M. Kareev, S. Middey, P. Kissin, *et al.*, Magnetic order driven ultrafast phase transition in NdNiO$_3$, Phys. Rev. B **106**, 165104 (2022).

[23] G. A. Pan, Q. Song, D. Ferenc Segedin, M.-C. Jung, H. El-Sherif, E. E. Fleck, B. H. Goodge, S. Doyle, D. Córdova Carrizales, A. T. N'Diaye, *et al.*, Synthesis and electronic properties of Nd$_{n+1}$Ni$_n$O$_{3n+1}$ Ruddlesden-Popper nickelate thin films, Phys. Rev. Mater. **6**, 055003 (2022).

[24] X. Granados, J. Fontcuberta, X. Obradors, L. Mañosa, and J. B. Torrance, Metallic state and the metal-insulator transition of NdNiO$_3$, Phys. Rev. B **48**, 11666 (1993).

[25] D. Kumar, K. P. Rajeev, J. A. Alonso, and M. J. Martínez-Lope, Slow dynamics in hard condensed matter: A case study of the phase separating system $NdNiO_3$, J. Phys.: Condens. Matter **21**, 185402 (2009).

[26] S. Chatterjee, R. S. Bisht, V. R. Reddy, and A. K. Raychaudhuri, Emergence of large thermal noise close to a temperature-driven metal-insulator transition, Phys. Rev. B **104**, 155101 (2021).

[27] G. L. Prajapati, S. Kundu, S. Das, T. D. V. V., and D. S. Rana, Hysteresis dynamics of rare earth nickelates: Unusual scaling exponent and asymmetric spinodal decomposition, New J. Phys. **24**, 103016 (2022).

[28] P. Majhi, S. Mitra, A. Singh, B. Ghosh, V. R. Reddy, S. Saha, and A. K. Raychaudhuri, Phase coexistence and resistance relaxation kinetics in $NdNiO_3$ films below the metal-insulator transition temperature, Phys. Rev. B **108**, 064103 (2023).

[29] L. Varbaro, L. Korosec, C.-Y. Hsu, D. T. L. Alexander, N. Jaouen, and J.-M. Triscone, Role of the coupling of the electronic transitions on the order of the metal-to-insulator phase transition in nickelates, APL Mater. **12**, 081120 (2024).

[30] X. Granados, J. Fontcuberta, X. Obradors, and J. B. Torrance, Metastable metallic state and hysteresis below the metal-insulator transition in $PrNiO_3$, Phys. Rev. B **46**, 15683 (1992).

[31] J. Pérez-Cacho, J. Blasco, J. García, M. Castro, and J. Stankiewicz, Study of the phase transitions in $SmNiO_3$, J. Phys.: Condens. Matter **11**, 405 (1999).

[32] P. C. Canfield, J. D. Thompson, S.-W. Cheong, and L. W. Rupp, Extraordinary pressure dependence of the metal-to-insulator transition in the charge-transfer compounds $NdNiO_3$ and $PrNiO_3$, Phys. Rev. B **47**, 12357 (1993).

[33] Y. Kumar, R. J. Choudhary, and R. Kumar, Strain controlled systematic variation of metal-insulator transition in epitaxial $NdNiO_3$ thin films, J. Appl. Phys. **112**, 073718 (2012).

[34] L. Wang, S. Ju, L. You, Y. Qi, Y.-W. Guo, P. Ren, Y. Zhou, and J. Wang, Competition between strain and dimensionality effects on the electronic phase transitions in $NdNiO_3$ films, Sci. Rep. **5**, 18707 (2015).

[35] M. Zaghrioui, A. Bulou, P. Lacorre, and P. Laffez, Electron diffraction and Raman scattering evidence of a symmetry breaking at the metal-insulator transition of $NdNiO_3$, Phys. Rev. B **64**, 081102(R) (2001).

[36] C. Girardot, J. Kreisel, S. Pignard, N. Caillault, and F. Weiss, Raman scattering investigation across the magnetic and metal-insulator transition in rare earth nickelate $R$$NiO_3$ (R = Sm, Nd) thin films, Phys. Rev. B **78**, 104101 (2008).

[37] I. Ardizzone, J. Teyssier, I. Crassee, A. B. Kuzmenko, D. G. Mazzone, D. J. Gawryluk, M. Medarde, and D. van der Marel, Raman spectroscopic evidence for multiferroicity in rare earth nickelate single crystals, Phys. Rev. Res. **3**, 033007 (2021).

[38] M. K. Stewart, J. Liu, M. Kareev, J. Chakhalian, and D. N. Basov, Mott physics near the insulator-to-metal transition in $NdNiO_3$, Phys. Rev. Lett. **107**, 176401 (2011).

[39] J. Ruppen, J. Teyssier, O. E. Peil, S. Catalano, M. Gibert, J. Mravlje, J.-M. Triscone, A. Georges, and D. van der Marel, Optical spectroscopy and the nature of the insulating state of rare-earth nickelates, Phys. Rev. B **92**, 155145 (2015).

[40] J. Bieder, A. Mercy, W.-Y. Tong, and P. Ghosez, Optical spectra of rare-earth nickelates, Phys. Rev. B **102**, 081111(R) (2020).

[41] See Supplemental Material at http://link.aps.org/supplemental/10.1103/yg97-vfmn for experimental details and additional results, which also includes Refs. [77–84].

[42] S. D. Brorson, A. Kazeroonian, J. S. Moodera, D. W. Face, T. K. Cheng, E. P. Ippen, M. S. Dresselhaus, and G. Dresselhaus, Femtosecond room-temperature measurement of the electron-phonon coupling constant γ in metallic superconductors, Phys. Rev. Lett. **64**, 2172 (1990).

[43] S. G. Han, Z. V. Vardeny, K. S. Wong, O. G. Symko, and G. Koren, Femtosecond optical detection of quasiparticle dynamics in high-T_c $YBaCu_3O_{7-\delta}$ superconducting thin films, Phys. Rev. Lett. **65**, 2708 (1990).

[44] W. Liang, H. Hou, Y. Lin, and S.-N. Luo, Ultrafast electron and spin dynamics of strongly correlated $NdNiO_3$, J. Phys. D **52**, 075303 (2019).

[45] A. Mann, E. Baldini, A. Odeh, A. Magrez, H. Berger, and F. Carbone, Probing the coupling between a doublon excitation and the charge-density wave in TaS_2 by ultrafast optical spectroscopy, Phys. Rev. B **94**, 115122 (2016).

[46] C. J. Sayers, A. Genco, C. Trovatello, S. D. Conte, V. O. Khaustov, J. Cervantes-Villanueva, D. Sangalli, A. Molina-Sanchez, C. Coletti, C. Gadermaier, *et al.*, Strong coupling of coherent phonons to excitons in semiconducting monolayer $MoTe_2$, Nano Lett. **23**, 9235 (2023).

[47] S. Mor, V. Gosetti, V. F. Agekyan, C. Giannetti, L. Sangaletti, and S. Pagliara, Effect of photoinduced screening on the spectroscopic signature of exciton-phonon coupling, ACS Photon. **11**, 2282 (2024).

[48] C. Slavov, H. Hartmann, and J. Wachtveitl, Implementation and evaluation of data analysis strategies for time-resolved optical spectroscopy, Anal. Chem. **87**, 2328 (2015).

[49] S. Borroni, E. Baldini, V. M. Katukuri, A. Mann, K. Parlinski, D. Legut, C. Arrell, F. van Mourik, J. Teyssier, A. Kozlowski, *et al.*, Coherent generation of symmetry-forbidden phonons by light-induced electron-phonon interactions in magnetite, Phys. Rev. B **96**, 104308 (2017).

[50] A. S. Johnson, D. Moreno-Mencía, E. B. Amuah, M. Menghini, J.-P. Locquet, C. Giannetti, E. Pastor, and S. E. Wall, Ultrafast loss of lattice coherence in the light-induced structural phase transition of V_2O_3, Phys. Rev. Lett. **129**, 255701 (2022).

[51] S. Mor, M. Herzog, J. Noack, N. Katayama, M. Nohara, H. Takagi, A. Trunschke, T. Mizokawa, C. Monney, and J. Stähler, Inhibition of the photoinduced structural phase transition in the excitonic insulator Ta_2NiSe_5, Phys. Rev. B **97**, 115154 (2018).

[52] C. J. Sayers, G. Marini, M. Calandra, H. Hedayat, X. Feng, E. van Heumen, C. Gadermaier, S. D. Conte, and G. Cerullo, Anomalous amplitude mode dynamics below the expected charge-density-wave transition in $1T$-VSe_2, Adv. Phys. Res. **4**, 2400114 (2025).

[53] A. D. Caviglia, R. Scherwitzl, P. Popovich, W. Hu, H. Bromberger, R. Singla, M. Mitrano, M. C. Hoffmann, S. Kaiser, P. Zubko, *et al.*, Ultrafast strain engineering in complex oxide heterostructures, Phys. Rev. Lett. **108**, 136801 (2012).

[54] E. Abreu, D. Meyers, V. K. Thorsmølle, J. Zhang, X. Liu, K. Geng, J. Chakhalian, and R. D. Averitt, Nucleation and growth bottleneck in the conductivity recovery dynamics of nickelate ultrathin films, Nano Lett. **20**, 7422 (2020).

[55] E. L. Ivchenko, *Optical Spectroscopy of Semiconductor Nanostructures* (Alpha Science International Ltd., Bromley, 2005).

[56] C. M. Nelson, M. Spies, L. S. Abdallah, S. Zollner, Y. Xu, and H. Luo, Dielectric function of $LaAlO_3$ from 0.8 to 6 eV between 77 and 700 K, J. Vac. Sci. Technol. A **30**, 061404 (2012).

[57] J. Blasco, M. Castro, and J. Garcia, Structural, electronic, magnetic and calorimetric study of the metal-insulator transition in $NdNiO_{3-\delta}$, J. Phys.: Condens. Matter **6**, 5875 (1994).

[58] V. B. Barbeta, R. F. Jardim, M. S. Torikachvili, M. T. Escote, F. Cordero, F. M. Pontes, and F. Trequattrini, Metal-insulator transition in $Nd_{1-x}Eu_xNiO_3$ probed by specific heat and anelastic measurements, J. Appl. Phys. **109**, 07E115 (2011).

[59] B. Torriss, A. Ibrahim, T. Ozaki, and M. Chaker, Ultrafast photoinduced insulator-metal transition in epitaxial samarium nickelate thin films investigated by time-resolved terahertz spectroscopy, Phys. Rev. B **98**, 165132 (2018).

[60] S. Wall, L. Foglia, D. Wegkamp, K. Appavoo, J. Nag, R. F. Haglund, J. Stähler, and M. Wolf, Tracking the evolution of electronic and structural properties of VO_2 during the ultrafast photoinduced insulator-metal transition, Phys. Rev. B **87**, 115126 (2013).

[61] D. Perez-Salinas, A. S. Johnson, D. Prabhakaran, and S. Wall, Multi-mode excitation drives disorder during the ultrafast melting of a C_4-symmetry-broken phase, Nat. Commun. **13**, 238 (2022).

[62] M. Hase, K. Ishioka, J. Demsar, K. Ushida, and M. Kitajima, Ultrafast dynamics of coherent optical phonons and nonequilibrium electrons in transition metals, Phys. Rev. B **71**, 184301 (2005).

[63] G. Mattoni, P. Zubko, F. Maccherozzi, A. J. H. van der Torren, D. B. Boltje, M. Hadjimichael, N. Manca, S. Catalano, M. Gibert, Y. Liu, *et al.*, Striped nanoscale phase separation at the metal-insulator transition of heteroepitaxial nickelates, Nat. Commun. **7**, 13141 (2016).

[64] D. Preziosi, L. Lopez-Mir, X. Li, T. Cornelissen, J. H. Lee, F. Trier, K. Bouzehouane, S. Valencia, A. Gloter, A. Barthélémy, *et al.*, Direct mapping of phase separation across the metal-insulator transition of $NdNiO_3$, Nano Lett. **18**, 2226 (2018).

[65] A. M. Alsaqqa, S. Singh, S. Middey, M. Kareev, J. Chakhalian, and G. Sambandamurthy, Phase coexistence and dynamical behavior in $NdNiO_3$ ultrathin films, Phys. Rev. B **95**, 125132 (2017).

[66] A. Volpato and E. Collini, Time-frequency methods for coherent spectroscopy, Opt. Express **23**, 20040 (2015).

[67] F. Vallée, Time-resolved investigation of coherent LO-phonon relaxation in III–V semiconductors, Phys. Rev. B **49**, 2460 (1994).

[68] D. Wegkamp, M. Herzog, L. Xian, M. Gatti, P. Cudazzo, C. L. McGahan, R. E. Marvel, R. F. Haglund, A. Rubio, M. Wolf, *et al.*, Instantaneous band gap collapse in photoexcited monoclinic VO_2 due to photocarrier doping, Phys. Rev. Lett. **113**, 216401 (2014).

[69] A. Cavalleri, T. Dekorsy, H. H. W. Chong, J. C. Kieffer, and R. W. Schoenlein, Evidence for a structurally-driven insulator-to-metal transition in VO_2: A view from the ultrafast timescale, Phys. Rev. B **70**, 161102(R) (2004).

[70] A. Singer, J. G. Ramirez, I. Valmianski, D. Cela, N. Hua, R. Kukreja, J. Wingert, O. Kovalchuk, J. M. Glownia, M. Sikorski, *et al.*, Nonequilibrium phase precursors during a photoexcited insulator-to-metal transition in V_2O_3, Phys. Rev. Lett. **120**, 207601 (2018).

[71] T. Amano *et al.*, Propagation of insulator-to-metal transition driven by photoinduced strain waves in a Mott material, Nat. Phys. **20**, 1778 (2024).

[72] P. V. Balachandran and J. M. Rondinelli, Interplay of octahedral rotations and breathing distortions in charge-ordering perovskite oxides, Phys. Rev. B **88**, 054101 (2013).

[73] K. Haule and G. L. Pascut, Mott transition and magnetism in rare earth nickelates and its fingerprint on the x-ray scattering, Sci. Rep. **7**, 10375 (2017).

[74] M. G. Cottam and D. J. Lockwood, Spin-phonon interaction in transition-metal difluoride antiferromagnets: Theory and experiment, Low Temp. Phys. **45**, 78 (2019).

[75] L. L. Hu, M. Yang, Y. L. Wu, Q. Wu, H. Zhao, F. Sun, W. Wang, R. He, S. L. He, H. Zhang, *et al.*, Strong pseudospin-lattice coupling in $Sr_3Ir_2O_7$: Coherent phonon anomaly and negative thermal expansion, Phys. Rev. B **99**, 094307 (2019).

[76] O. Dogadov, Dataset for "Ultrafast modification of coherent phonons during the photoinduced insulator-to-metal phase transition in neodymium nickelate" [Data set], Zenodo (2025), doi: 10.5281/zenodo.17791567.

[77] N. E. Massa, J. A. Alonso, M. J. Martínez-Lope, and I. Rasines, Reflectivity, transmission, and photoinduced infrared spectra of $NdNiO_3$, Phys. Rev. B **56**, 986 (1997).

[78] T. Willett-Gies, E. DeLong, and S. Zollner, Vibrational properties of bulk $LaAlO_3$ from Fourier-transform infrared ellipsometry, Thin Solid Films **571**, 620 (2014).

[79] C. Manzoni and G. Cerullo, Design criteria for ultrafast optical parametric amplifiers, J. Opt. **18**, 103501 (2016).

[80] E. Knoesel, A. Hotzel, and M. Wolf, Ultrafast dynamics of hot electrons and holes in copper: Excitation, energy relaxation, and transport effects, Phys. Rev. B **57**, 12812 (1998).

[81] A. Villa, A. M. Ross, R. Gotti, M. Lamperti, F. Scotognella, G. Cerullo, and M. Marangoni, Broadly tunable mid-infrared femtosecond pulses directly generated by an optical parametric amplifier, OSA Continuum **4**, 2837 (2021).

[82] A. Othonos, Probing ultrafast carrier and phonon dynamics in semiconductors, J. Appl. Phys. **83**, 1789 (1998).

[83] S. Hunsche, K. Wienecke, T. Dekorsy, and H. Kurz, Impulsive softening of coherent phonons in tellurium, Phys. Rev. Lett. **75**, 1815 (1995).

[84] P. Ruello and V. E. Gusev, Physical mechanisms of coherent acoustic phonons generation by ultrafast laser action, Ultrasonics **56**, 21 (2015).